



Temperature-dependent coherence properties of NV ensemble in diamond up to 600 KShengran Lin , Changfeng Weng, Yuanjie Yang, Jiaxin Zhao, Yuhang Guo,
Jian Zhang, Liren Lou, Wei Zhu, and Guanzhong Wang *Key Laboratory of Strongly-Coupled Matter Physics, Chinese Academy of Sciences, Hefei National Laboratory for Physical Science at Microscale, and Department of Physics, University of Science and Technology of China, Hefei, Anhui, 230026, People's Republic of China*

(Received 25 February 2021; revised 9 June 2021; accepted 4 October 2021; published 26 October 2021)

The nitrogen-vacancy (NV) center in diamond is an ideal candidate for quantum sensing because of its excellent spin coherence property as well as the possibility for optical initialization and readout. Previous studies, on the other hand, have typically been conducted at low or room temperature. The inability to fully understand the coherence properties of the NV center at high temperatures limits NV's further applications. We systematically investigate the coherence properties of NV center ensemble at temperatures ranging from 300 K to 600 K in this paper. Coherence time T_2 decreases rapidly from 184 μs at 300 K to 30 μs at 600 K due to the interaction with paramagnetic impurities. At all experiment temperatures, both single-quantum and double-quantum transitions exhibit a T^5 relaxation rate, which is attributed to the two-phonon Raman process. Nonetheless, the inhomogeneous dephasing time T_2^* and thermal-echo decoherence time T_{TE} remain almost unchanged at temperature up to 600 K. A thermal-echo-based thermometer is demonstrated to have a sensitivity of 41 mK/ $\sqrt{\text{Hz}}$ at 450 K. These findings will pave the way for NV-based high-temperature sensing and provide a more comprehensive understanding of solid-state qubit decoherence.

DOI: [10.1103/PhysRevB.104.155430](https://doi.org/10.1103/PhysRevB.104.155430)**I. INTRODUCTION**

The negatively charged nitrogen-vacancy (NV) center in diamond has gotten a lot of interest because of its outstanding room-temperature characteristics, such as long spin coherence time, optical state initialization and readout, and sensitivity to various external fields [1]. These characteristics make it a promising contender for applications ranging from quantum information processing [2] to quantum computing [3] to quantum sensing [1,4–7]. Relative to conventional sensors, NV-based sensors excel in high spatial resolution [5], broad bandwidth [6,8], and multifield sensing [1,4–7]. Diamond's excellent thermal conductivity and stability, in particular, allow NV-based sensors to operate at high temperatures [9,10]. It is pointed out that the NV center can be coherently controlled and maintain a long inhomogeneous dephasing time at temperatures up to 625 K [9]. By initializing and reading at room temperature, one can manipulate the NV center at temperatures up to 1000 K [10], which is above the working temperature of most nanosensors. As a result, the NV center is an appealing broad-temperature-range quantum sensor that can be used to investigate temperature-related phenomena such as temperature-dependent magnetic properties of nanoparticles [11], thermoelectric effects [12], and spin-wave propagation above ambient temperature [13].

The coherence time of NV center, like inhomogeneous dephasing time T_2^* for DC measurement and relaxation time T_1 and coherence time T_2 for AC measurement, is an important parameter linked to sensitivity for NV-based sensors. Prior

studies of NV center at high temperatures, however, have mostly focused on T_1 and T_2^* [9,10,14], with little knowledge about T_2 , which not only limits the maximum number of gate operations in quantum computing [3] or quantum information processing [2] but also determines the sensitivity of the associated sensor for AC measurement (magnetic field [6], electric field [15], electron spin [16], and nuclear spin [17]) and echo-type thermometry (thermal-echo and T-CPMG protocol [7,18]). Furthermore, the double-quantum (DQ) relaxation, which exists in the three-level spin system [Fig. 1(a)] of the NV center ground state, is thought to have a substantial influence on the decoherence of the NV center. Recent study indicates that at low magnetic field, DQ relaxation will dominate the decoherence of near-surface NV center [19]. Nonetheless, the origin of DQ relaxation remains a mystery. Determining the temperature dependency of DQ relaxation may help to identify the question. For potential future uses, a thorough research of the coherence properties of the NV center at high temperatures is required. Besides, the majority of the research makes use of a single NV center. The utilization of NV center ensemble will improve the sensitivity and signal-to-noise (SNR) of the NV-based sensor [20], as well as provide a platform for investigating the quantum many-body spin physics at high temperatures [21].

In this paper, we systematically investigate the coherence properties of the NV center ensemble at temperatures ranging from 300 K to 600 K. The spin-echo pulse experiments indicate that when temperature rises, the coherence time T_2 decreases rapidly. In contrast, the inhomogeneous dephasing time T_2^* remains almost unchanged, despite a reduction in optically detected magnetic resonance (ODMR) contrast. As temperatures rise, the single-quantum (SQ) and DQ relaxation

*gzwang@ustc.edu.cn

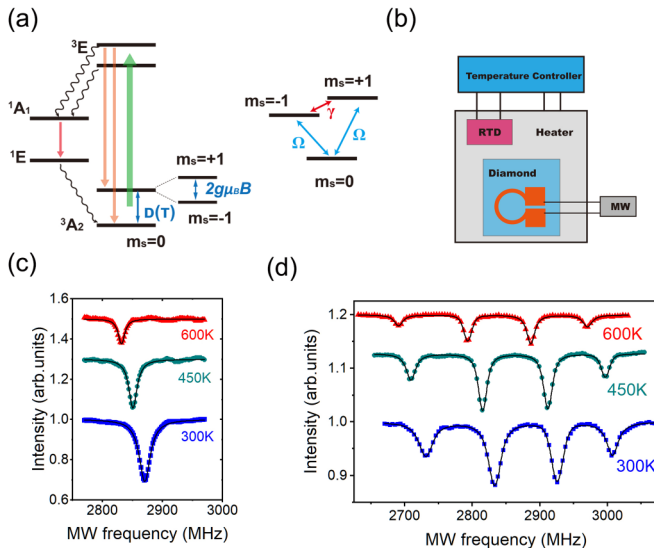


FIG. 1. (a) Left: The electronic energy level diagram for the NV center; the degenerated sublevel $|m_s = \pm 1\rangle$ is split with the magnetic field applied. The straight lines represent optical transitions, and the snaked lines represent nonradiative decay. Right: Ground state energy level of the NV center. The blue arrows indicate the single-quantum channel, and the corresponding relaxation rate is Ω (here we set $\Omega_{0,+1} = \Omega_{0,-1} = \Omega$, as verified experimentally in Ref. [19]). The red arrow indicates the double-quantum channel, and the corresponding relaxation rate is γ . (b) Schematic showing the experimental arrangement of the sample and the heating part. The diamond sample is adhered to a resistance heating plate with the temperature detected by a resistive temperature detector (RTD) and controlled with a temperature controller. A ring-shaped antenna is set on the sample to deliver the MW field. (c) Zero field CW ODMR spectra at three temperatures, 300 K, 450 K, 600 K (from the bottom up). (d) CW ODMR at three temperatures with a 50 G magnetic field applied.

rates both increase fast. Being the simplest echo-type temperature sensing protocol [7], thermal-echo (TE) sequence is immune to static magnetic fields and low-frequency magnetic noise. We conducted the TE measurement at high temperatures, and the associated decoherence time T_{TE} remains nearly unchanged. We also performed the high-temperature thermometry based on NV center ensemble at around 450 K. These discoveries will motivate the utilization of NV-based devices in high-temperature applications.

II. EXPERIMENT

A diamond plate sample grown by plasma-enhanced CVD is used in the experiment ($[N] \approx 125$ ppb, $[NV^-] \approx 2$ ppb ($1 \text{ ppb} = 1.76 \times 10^{14}/\text{cm}^3$)). The concentration of nitrogen was determined by electron paramagnetic resonance (EPR, JES-FA200), and the concentration of NV center was estimated by comparing the photoluminescence (PL) intensity of the sample to that of a single NV center. We used a home-built confocal microscope (CFM) equipped with a microwave (MW) system to manipulate the NV center coherently. A 532 nm laser was used to excite the NV center, with the resulting fluorescence collected and directed to a single pho-

ton counter (SPCM-AQRH-W4). To avoid the effect of laser heating on the diamond plate, we kept the power of the laser beam ahead of the objective lens at 0.2 mW in all the subsequent measurements. The MW was delivered to the NV center through the ring-shaped coplanar waveguide on the diamond plate [Fig. 1(b)]. More detail of the setup can be found in our previous report [18]. To investigate the temperature-dependent coherence property of the NV center, a metal-ceramic heater (HT24S, Thorlabs) attached to the diamond and a resistive temperature detector (TH100PT, Thorlabs) fixed closely to the diamond were employed to adjust the temperature of the diamond [Fig. 1(b)].

As shown in Fig. 1(c), the zero-field continuous-wave (CW) ODMR spectra of NV center exhibit a resonance peak, corresponding to the zero-field splitting (ZFS) between the $m_s = \pm 1$ and $m_s = 0$ spin sublevels of NV center [hereafter we use the letter ‘D’ to denote the value of ZFS, see Fig. 1(a)]. Both D and ODMR contrast decrease as temperature rises, with the former attributed to thermal expansion and electron-phonon interaction [9,22,23] and the latter to enhanced nonradiative relaxation of the $m_s = 0$ state [9]. The temperature dependence of D varies little among diamond samples, according to our experiment and the results reported in the literature [9,23,24]. Thus, in the subsequent experiments, we used the $D(T)$ relationship reported in Ref. [9] to determine the temperature, which was also confirmed by the temperature dependence of the diamond Raman shift [25].

We then conducted pulse ODMR experiments to extract the coherence times of the NV center at various temperatures. To lift the degeneracy of the $m_s = \pm 1$ spin sublevels and to spectrally distinguish the NV center with different crystallographic orientations, a magnetic field of about 50 G was applied by using a high-temperature magnet ($\text{Sm}_2\text{Co}_{17}$), with the magnetic field direction adjusted to be parallel to one of the $\langle 111 \rangle$ directions of the diamond sample. The corresponding CW spectrum contains four resonances [Fig. 1(d)], and we chose the two most outer resonances, which belong to the NV center with the axes parallel to the magnetic field direction, to be used in the following experiment. Then we applied various pulse sequences to obtain the relevant coherence times.

III. RESULT AND DISCUSSION

A. Ramsey and thermal-echo measurement

Ramsey and TE [7] pulse sequences are widely used in quantum sensing, with the associated coherence times, inhomogeneous dephasing time T_2^* and TE dephasing time T_{TE} , being crucial parameters relating to the sensing sensitivity. T_2^* is defined as the time after which the qubit superposition’s coherence decays from 1 to $1/e$. Figure 2(a) depicts the Ramsey measurement pulse sequence. The two laser pulses at the start and the end of the sequence are used to polarize and read the spin state of NV center, respectively. Resonant MW pulses were used to manipulate the NV center coherently. The first MW $\pi/2$ pulse is used to transfer the NV $|0\rangle$ state into a superposition state such as $|\phi\rangle = 1/\sqrt{2}(|0\rangle + |-1\rangle)$ or other equilibrium states, and the second MW $\pi/2$ pulse

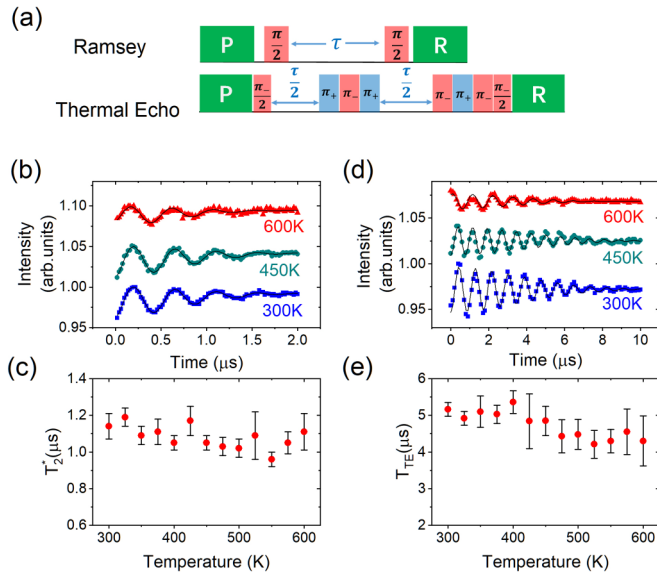


FIG. 2. Ramsey and thermal echo measurement. (a) Pulse sequence for Ramsey and thermal echo, respectively. Upper panel: Ramsey; lower panel: thermal echo. Minus (−) denotes the transition $|0\rangle \leftrightarrow |-1\rangle$, and plus (+) denotes the transition $|0\rangle \leftrightarrow |+1\rangle$. (b) Ramsey fringes at 300 K, 450 K, and 600 K (from the bottom up). The solid line represent the fitting curves. The fitting R squares are $R^2 = 0.92, 0.95, 0.83$ from the bottom up. (c) Inhomogeneous dephasing time T_2^* from 300 K to 600 K. (d) Thermal echo curves at 300 K, 450 K, and 600 K (from the bottom up). The solid lines represent the fitting curves ($R^2 = 0.94, 0.90, 0.84$, from the bottom up). (e) Thermal echo coherence time T_{TE} from 300 K to 600 K. Error bars in (c) and (e) represent one standard deviation found from the fitting.

is used to convert the accumulated phase into population difference, which can be read out optically. By varying the interval between two MW pulses, we will obtain the Ramsey fringe and the corresponding inhomogeneous dephasing time.

In the experiment, we carried out Ramsey measurement at temperatures ranging from 300 K to 600 K, and the results are given in Fig. 2(b). The data are fitted by the function $a \exp[-(t/T_2^*)^n] * \cos(2\pi f_0 t + \varphi) + b$, where a, b, φ are free parameters, n is the stretched exponential parameter depending on the specific noise source, T_2^* is the inhomogeneous dephasing time, and $f_0 = 2.2$ MHz is the MW detuning result from the coupling with ^{14}N nuclear spin (the MW frequency is set on the resonance with the $m_I = 0$ transition). The oscillation of the curves was ascribed to the MW frequency detuning from the resonance and the interaction with ^{14}N nuclear spin. The contrast decreases as temperature rises, while the dephasing time T_2^* remains nearly constant [Fig. 2(c)]. We also conducted TE measurement at various temperature, with the measurement pulse sequence shown in Fig. 2(a). For the TE measurement, both $|0\rangle \leftrightarrow |-1\rangle$ and $|0\rangle \leftrightarrow |+1\rangle$ transitions were utilized to reduce the dephasing effect from the stray magnetic field, thus a longer dephasing time can be obtained comparing to the T_2^* derived from Ramsey measurement. The TE curves at three different temperatures (300 K, 450 K, 600 K) are depicted in Fig. 2(d). We used the function $a \exp[-(t/T_{TE})^n] * \cos(2\pi f t + \varphi) + b$ to fit the data, where

a, b, φ are free parameters, n is the stretched exponential parameter, T_{TE} is thermal-echo dephasing time, and oscillation frequency $f = (w_+ - w_-)/2 - D$, in which w_+ and w_- are the applying MW frequencies, and D is the zero-field splitting of the NV center ground state. Figure 2(e) summarizes the T_{TE} from 300 K to 600 K, which keep nearly unchanged as well.

^{13}C nuclear spins are the primary dephasing source responsible for T_2^* in the diamond sample we used in this study. Because the experiment temperatures are well above the polarization temperature of ^{13}C nuclear spin ($k_B T \gg \mu_I B$, in which k_B is the Boltzmann constant, μ_I is the nuclear magnetic moment of ^{13}C , and B is the magnitude of magnetic field), ^{13}C nuclear spins are assumed to have an equal population at each sublevel. Moreover, recent research indicates that the hyperfine interaction between the NV electron spin and the ^{13}C nuclear spin remains almost unaltered at temperatures up to 700 K [26]. As a result, the dephasing effect of the ^{13}C nuclear spin bath is nearly temperature independent, leading to a temperature-independent T_2^* . The robustness of T_{TE} should be explained by the same process. These results show that the Ramsey-based or TE-based NV sensor can operate reliably at temperatures as high as 600 K.

B. Relaxation and spin-echo measurement

1. Relaxation

We then conducted relaxation and spin-echo measurements to determine the relaxation rate and coherence time T_2 . The relaxation rate is a measure of how quickly the population recovers to equilibrium, and it sets the upper limit of coherence time T_2 [19]. Because the DQ transition ($\Delta m = \pm 2$) will contribute to the NV center's relaxation process [19], the DQ relaxation rate is also determined. In this work, SQ transition denotes the transition between $m_s = 0$ and $m_s = -1$ states, while DQ transition denotes the transition between $m_s = -1$ and $m_s = +1$ states. To extract the SQ relaxation rate Ω and DQ relaxation rate γ , state-selective π pulses are utilized to measure the population dynamics into and out of each spin sublevel (MW π_- pulses will exchange the population between $m_s = -1$ and $m_s = 0$ states, and MW π_+ pulses will exchange the population between $m_s = +1$ and $m_s = 0$ states). The standard sequences for measuring Ω and γ are shown in Fig. 3(a) and Fig. 3(b). According to the solution of the $|m_s\rangle$ states population dynamic equations, applying these two sequences yields relaxation signals well fitted by functions $S_1(\tau) = r \exp(-3\Omega\tau)$ and $S_2(\tau) = r \exp[-(\Omega + 2\gamma)\tau]$, respectively (r is the fluorescence contrast) [19]. Thus, the transition rates Ω and γ can be obtained by fitting the relaxation curves.

The relaxation curves obtained using the sequence in Fig. 3(a) [Fig. 3(b)] at three representatives temperatures (300 K, 450 K, 600 K) are shown in Fig. 3(c) [Fig. 3(d)]. The associated relaxation rates are acquired by fitting the curves as mentioned above. Figure 3(e) depicts that the SQ relaxation rates are well fitted by function $A_\Omega T^5 + B_\Omega$, with $A_\Omega = 1.46(7) \times 10^{-11} \text{ K}^{-5} \text{ s}^{-1}$ and $B_\Omega = 79(7) \text{ s}^{-1}$, indicating that the SQ relaxation is dominated by a two-phonon Raman process [10,14,27]. Figure 3(f) summarizes the DQ transition rate γ at temperatures ranging from 300 K to 600 K, which are fitted quite well by the function $A_\gamma T^5 + B_\gamma$. The

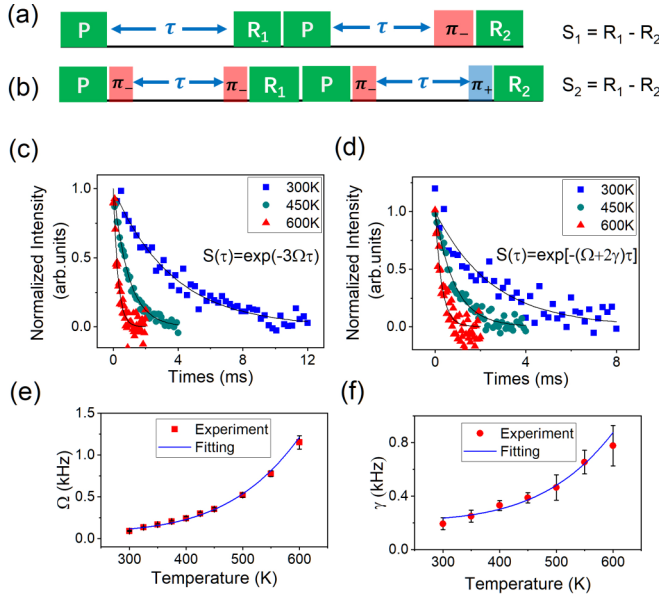


FIG. 3. DQ and SQ relaxation experiment. (a),(b) Measurement sequences to extract the relaxation rate Ω and γ . Minus (-) denotes the transition $0 \leftrightarrow -1$, and plus (+) denotes the transition $0 \leftrightarrow +1$. (c) Relaxation curves acquired by using the sequence in (a) at 300 K, 450 K, 600 K, respectively. The data are fitted with function $\exp(-3\Omega\tau)$, with the fitting R square being 0.96 (300 K), 0.98 (450 K), and 0.92 (600 K). Since spin-lattice relaxation T_1 is the time it takes for the curves to decay to $1/e$ of its initial value, we will have $T_1 = 1/3\Omega$. (d) Relaxation curves acquired by using the sequence in (b) at 300 K, 450 K, and 600 K, respectively. The data are fitted by function $\exp[-(\Omega + 2\gamma)\tau]$, with the fitting R square being 0.88 (300 K), 0.96 (450 K), and 0.88 (600 K). (e) Temperature dependence of single-quantum relaxation rate Ω . Red points are experiment data, and the blue solid line is the fitting curve [$A_\Omega T^5 + B_\Omega$, with $A_\Omega = 1.46(7) \times 10^{-11} \text{ K}^{-5} \text{ s}^{-1}$ and $B_\Omega = 79(7) \text{ s}^{-1}$]. The fitting R square is $R^2 = 0.98$. (f) Temperature dependence of double-quantum relaxation rate γ . Red points are experimental data, and the solid line is the fitting curve [$A_\gamma T^5 + B_\gamma$, with $A_\gamma = 0.85(9) \times 10^{-11} \text{ K}^{-5} \text{ s}^{-1}$ and $B_\gamma = 215(20) \text{ s}^{-1}$]. The fitting R square is $R^2 = 0.93$. The error bars in (e) and (f) represent one standard deviation found from the fitting.

fitting values are $A_\gamma = 0.85(9) \times 10^{-11} \text{ K}^{-5} \text{ s}^{-1}$ and $B_\gamma = 215(20) \text{ s}^{-1}$. According to the T^5 temperature scaling, the DQ relaxation may also be dominated by a two-phonon Raman process, which is consistent with Walker's result [27].

2. Spin-echo measurement

The coherence time T_2 is defined as the time to loss of coherence from 1 to $1/e$ when control pulses are applied during the total precession period. The use of control pulses allows the dephasing caused by stray fields to be refocused, resulting in a longer dephasing time. The most basic case is the spin echo, where a π pulse is applied in the middle of the free evolution duration. To eliminate common-mode noise, we performed the spin-echo measurement using the sequence shown in Fig. 4(a). Figure 4(b) shows the spin-echo curves at four representative temperatures (300 K, 400 K, 500 K,

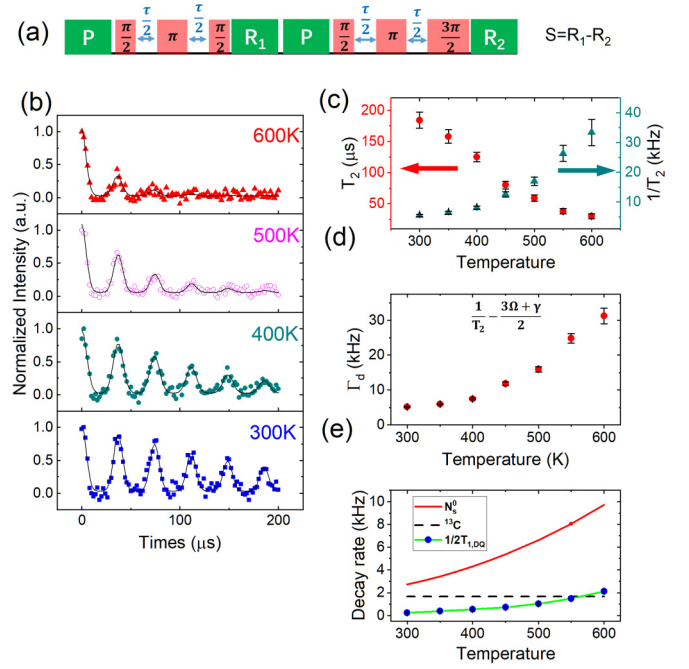


FIG. 4. Spin-echo measurement. (a) Pulse sequences for spin-echo measurement. (b) Spin-echo curves at four temperatures: 300 K, 400 K, 500 K, 600 K (from the bottom up). The experiment data are fitted by function $\exp[-(\tau/T_2)^p] \times \sum_i \exp[-(\tau - i \times T_R)^2/T_w^2]$, with p , T_R , T_w being the fit parameters. The fitting R square is $R^2 = 0.91, 0.91, 0.90, 0.85$ (from the bottom up). (c) The temperature dependence of coherence time T_2 (decoherence rate $1/T_2$). (d) The temperature dependence of pure dephasing rate, $\Gamma_d = 1/T_2 - (3\Omega + \gamma)/2$. (e) The temperature dependence of decoherence effect from relaxation (blue dots), P1 center (red solid line), ^{13}C nuclear spin (black dashed line). The contribution from P1 center and ^{13}C nuclear spin are estimated from Eq. (2) and Eq. (3), while the contribution from the relaxation is determined from the experiment. Error bars represent one standard deviation found from fitting.

600 K). The signal's collapses and revivals are attributed to the interactions with the nuclear spin of ^{13}C in diamond, with the revival period being $T_R = 2000/(\gamma_{^{13}\text{C}}B)$ ($\gamma_{^{13}\text{C}} = 1.071$ is the gyromagnetic ratio of nuclear ^{13}C and B is the magnitude of the applied magnetic field). To obtain T_2 , we fitted the data with function $\exp[-(\tau/T_2)^p] \times \sum_i \exp[-(\tau - i \times T_R)^2/T_w^2]$, where p is the stretched exponential parameter, T_2 is spin-echo coherence time, T_w is the relaxation time of the first collapse, and T_R is the period of the revival. Unlike the robust behavior of T_2^* and T_{TE} , T_2 decrease almost linearly from 184 μs at 300 K to 30 μs at 600 K [Fig. 4(c)]. T_2 can be restored to its original value after the sample has cooled (data not shown here).

For a three-level system, the constraint of T_2 is [19]

$$\frac{1}{T_2} = \Gamma_d + \frac{3\Omega + \gamma}{2} \quad (1)$$

where Γ_d is the pure dephasing rate, and $(3\Omega + \gamma)/2$ is the contribution from lifetime broadening, with DQ relaxation taken into account. Because our findings show that Ω and γ are both temperature dependent, lifetime broadening will con-

tribute to T_2 decrease as temperature rises. We subtracted the corrected relaxation rate $[(3\Omega + \gamma)/2]$ from the measured decoherence rate ($1/T_2$) to determine the temperature behavior of pure dephasing. Figure 4(d) shows that the pure dephasing rate Γ_d increases as temperature rises. For the NV center in diamond, the primary dephasing mechanism is the dipolar interaction with the surrounding spins, whose flip causes fluctuations of the local field around the NV center. Spins can flip in two ways: spin-lattice (SL) relaxation and spin-spin (SS) relaxation. In the former case, a spin changes from α state to β state, whereas in the latter case, a pair of spins exchange their states simultaneously, resulting in the so-called flip-flop process (α and β indicate different spin sublevels of the spin). The corresponding contributions from these two processes to the dephasing are given by [28]

$$\frac{1}{T_{SL}} = \frac{1}{1.4} \left(\frac{2.53\mu_0 g_e g_A \beta_e \beta_A c_A}{4\pi \hbar T_1^A} \right)^{1/2} \quad (2)$$

$$\frac{1}{T_{SS}} = \frac{0.37\mu_0 (g_e \beta_e)^{1/2} (g_A \beta_A)^{3/2} [S(S+1)]^{1/4}}{2} c_A \quad (3)$$

in which A denotes specie of the surrounding spins, $\mu_0 = 4\pi \times 10^{-7} T^2 J^{-1} m^3$ is the permeability of vacuum, $g_e = 2$ is the g factor of NV center, g_A is the g factor of A spins, β_e is the Bohr magneton, β_A is Bohr magneton or nuclear magneton, depending on the spin type being electron spin or nuclear spin, c_A is the volume number density of A spins in diamond, and T_1^A is the longitudinal relaxation time of A spins. Equation (3) indicates that $1/T_{SS}$ is temperature independent under the condition that the experiment temperatures are well above the polarization temperature of A spins. For the diamond sample used in this work, the main paramagnetic impurities are the electron spin of substitutional nitrogen ($[N_s^0] = 125$ ppb, P1 center) and the nuclear spin of ^{13}C ($[^{13}C] \approx 1.1\%$). Schematically, the pure dephasing rate of the NV center can be expressed as [29]

$$\Gamma_d = \frac{1}{T_2, \{N_s^0\}} + \frac{1}{T_2, \{^{13}C\}} + \frac{1}{T_2, \{\text{others}\}} \quad (4)$$

for ^{13}C nuclear spin, the longitudinal relaxation time is fairly long, thus the contribution from spin-lattice relaxation can be neglected, $\frac{1}{T_2, \{^{13}C\}} \approx \frac{1}{T_{SS, \{^{13}C\}}}$. For the P1 center, the longitudinal relaxation is dominated by spin-orbit phonon-induced tunneling at high temperatures, with $1/T_1^N = A_N T + B_N T^5$ (T is the temperature; A_N and B_N are constants) [30]. In this paper, we used $A_N = 5 \times 10^{-5} \text{ K}^{-1} \text{ s}^{-1}$, $B_N = 1.1 \times 10^{-10} \text{ K}^{-5} \text{ s}^{-1}$ to calculate the $1/T_{SL}, \{N_s^0\}$ (the parameters are extracted from Ref. [30], with the diamond P1 center concentration nearly equal to that of our diamond sample). Figure 4(e) illustrates the decoherence effect caused by the ^{13}C nuclear spin and the P1 center, respectively. The P1 center is clearly the dominant decoherence source, with the decoherence rate increasing rapidly as temperature rises while the contribution of ^{13}C nuclear to decoherence remains unchanged. The contribution from lifetime broadening is also shown, but it is minor in comparison to other effects. Because the relaxation rates exhibit T^5 behavior, it is expected to have a significant impact on the decoherence of NV center at higher temperatures. The decoherence effect, however, cannot

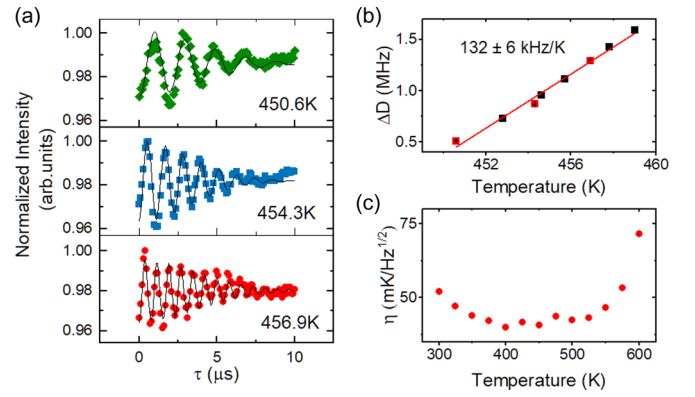


FIG. 5. Thermal echo based thermometry. (a) Thermal echo curves at three temperatures (456.9 K, 454.3 K, and 450.6 K, from the bottom up), with the applied microwave frequencies fixed. Solid lines are fitting curves. (b) Temperature dependence of thermal echo curve oscillation frequency. The red solid line is a linear fitting ($R^2 = 0.98$), with a slope of 132 ± 6 kHz/K. The red points indicate the data extract from (a). (c) The thermal sensitivity obtained from Eq. (5), with all parameters determined from the experiment.

fully represent the decrease of T_2 as temperature rises. This discrepancy was attributed to other paramagnetic impurities found in CVD diamond that we did not consider here, such as NVH [31], vacancy cluster [32], and SiV^- [33] *et al.*

IV. HIGH TEMPERATURE THERMOMETRY

Since the NV center's TE dephasing time is invariant at temperatures up to 600 K, we demonstrate the NV-ensemble-based high-temperature thermometry by using the TE technique. The basis of NV center temperature sensing is to determine the shift of D as temperatures change. In the TE protocol [pulse sequence shown in the lower panel of Fig. 2(a)], the NV center is first initialized into superposition of two of its three spin sublevels, like $1/\sqrt{2}(|0\rangle + |-1\rangle)$ in this paper. After half of the total free evolution time, a triple echo pulse sequence of the form $\pi_+ \pi_- \pi_+$ is applied to swap the population between the $m_s = -1$ and $m_s = +1$ states, where the π_{\pm} represents the MW π pulse used to manipulate the $|m_s = 0\rangle \leftrightarrow |m_s = \pm 1\rangle$ transitions and then undergo the left half of the total free evolution period; another triple pulse $\pi_- \pi_+ \pi_-$ is applied to change the NV center back into $\{m_s = 0, m_s = -1\}$ subspace, with a total phase factor e^{-iDt} accumulated, which is independent of inhomogeneous magnetic field or slowly-changing magnetic noise [7]. Finally, a $(\pi_-/2)$ pulse is used to convert the phase factor into population difference, allowing the phase factor to be read out optically. The prototype thermometer was tested at temperatures around 450 K. In the experiment, the MW frequencies remained constant. The D value was determined using the oscillation frequency of the thermal-echo curve [$f = (\omega_- + \omega_+)/2 - D$, in which ω_- and ω_+ are applied MW frequencies]. Figure 5(a) depicts three representatives thermal-echo curves measured at different temperatures (450.6 K, 454.3 K, and 456.9 K), which exhibit oscillation at frequencies of 1295 kHz, 870 kHz, and 512 kHz, respectively. Figure 5(b) shows that the oscillation frequencies are linearly dependent on temperature with a slope of 132 ± 6 kHz/K, which is consistent with the

temperature dependency of D [9]. To evaluate the sensitivity of our TE based thermometry, we use the equation [7]

$$\eta = \sqrt{\frac{2(p_0 + p_1)^2}{p_0 - p_1}} \frac{1}{2\pi \frac{dD}{dT} \exp\left(-\left(\frac{t}{T_{TE}}\right)^m\right) \sqrt{t}} \quad (5)$$

in which p_0 and p_1 are photo count per measurement shot of the NV ensemble in the bright and dark state, respectively, T_{TE} is the TE dephasing time, D is the zero-field splitting, and the sensitivity corresponds to the maximum value of $\exp\left[-\left(\frac{t}{T_{TE}}\right)^m\right] \sqrt{t}$. The number of NV centers in the confocal volume is estimated to be 350 by comparing the intensity of the sample's photoluminescence to that of a single NV center, and only one quarter contributes to the thermometry. We determined the sensitivity to be about 41 mK/ $\sqrt{\text{Hz}}$ at 450 K, superior to that of single NV center [7,9] and an order of magnitude larger than that in SiC [34]. Based on the T_{TE} obtained in previous experiments [Fig. 2(e)], we determined our thermometer's temperature sensitivity at temperatures ranging from 300 K to 600 K [Fig. 5(c)] using the values of dD/dT obtained from the $D(T)$ relationship reported in Ref. [9]. We found that the sensitivity was maximum at temperatures ranging from 400 K to 500 K and that it was restricted at higher temperatures due to the decrease in fluorescence intensity and ODMR contrast of the NV center [9]. The sensitivity of our sample is limited by the coherence time and concentration of the NV center. Due to the interaction with ^{13}C nuclear spins, the TE protocol only utilizes the first coherence collapse in the spin-echo measurement [7], resulting in a short coherence time. The ^{12}C -purified technique not only eliminates the ^{13}C -lead collapse but also significantly increases the coherence time [35], which improves sensitivity by at least an order of magnitude. The dynamical decoupling method [36,37] has also been shown to be effective in extending the coherence time of the NV center. According to Ref. [18], the coherence time for high-order TCPMG can be increased to 108 μs , which is approximately 11 times the value 9.5 μs for the TE method. Increased NV center concentration can also

improve the sensitivity, but the corresponding coherence time is usually short due to the accompanying high concentrations of paramagnetic defect (like P1 center.). As a result, it is proposed to increase the concentration of the NV center while keeping the concentrations of other paramagnetic defects constant, such as improving the nitrogen-to-NV conversion efficiency via annealing or electron irradiation. Because only one fourth of the NV centers contribute to the signal contrast in the pulse ODMR protocols, using preferred-aligned NV ensemble [38,39] will significantly improve ODMR contrast and sensitivity.

V. CONCLUSION

In conclusion, we determined the temperature dependence of NV ensemble coherence properties from 300 K to 600 K. The results reveal that the inhomogeneous dephasing time T_2^* and thermal echo decoherence time T_{TE} are robust to temperature variation. Taking advantage of this robust behavior, the TE-based thermometry exhibits a sensitivity of 41 mK/ $\sqrt{\text{Hz}}$ at 450 K. However, as temperature rises, the SQ and DQ relaxation rates increase rapidly, which is attributed to the spin-phonon interaction. Furthermore, we report the coherence time T_2 of the NV center ensemble at temperatures up to 600 K. The findings suggest that paramagnetic impurities will have a significant impact on the spin coherence of the NV center at high temperatures. We believe that the investigation of the high-temperature spin coherence properties of the NV center will not only broaden the applications of NV-based sensors but also provide a complete understanding of decoherence in the NV center or other solid qubits, such as the divacancy center in silicon carbide (SiC) [34].

ACKNOWLEDGMENTS

This work was supported by the National Natural Science Foundation of China (Grants No. 11374280 and No. 50772110). This work was partially carried out at the USTC Center for Micro and Nanoscale Research and Fabrication.

-
- [1] R. Schirhagl, K. Chang, M. Loretz, and C. L. Degen, Nitrogen-vacancy centers in diamond: Nanoscale sensors for physics and biology, *Annu. Rev. Phys. Chem.* **65**, 83 (2014).
- [2] T. van der Sar, Z. H. Wang, M. S. Blok, H. Bernien, T. H. Taminiau, D. M. Toyli, D. A. Lidar, D. D. Awschalom, R. Hanson, and V. V. Dobrovitski, Decoherence-protected quantum gates for a hybrid solid-state spin register, *Nature (London)* **484**, 82 (2012).
- [3] R.-B. Liu, W. Yao, and L. Sham, Quantum computing by optical control of electron spins, *Adv. Phys.* **59**, 703 (2010).
- [4] F. Dolde, H. Fedder, M. W. Doherty, T. Nöbauer, F. Rempp, G. Balasubramanian, T. Wolf, F. Reinhard, L. C. L. Hollenberg, F. Jelezko, and J. Wrachtrup, Electric-field sensing using single diamond spins, *Nat. Phys.* **7**, 459 (2011).
- [5] G. Balasubramanian, I. Y. Chan, R. Kolesov, M. Al-Hmoud, J. Tisler, C. Shin, C. Kim, A. Wojcik, P. R. Hemmer, A. Krueger, T. Hanke, A. Leitenstorfer, R. Bratschitsch, F. Jelezko, and J. Wrachtrup, Nanoscale imaging magnetometry with diamond spins under ambient conditions, *Nature (London)* **455**, 648 (2008).
- [6] J. R. Maze, P. L. Stanwix, J. S. Hodges, S. Hong, J. M. Taylor, P. Cappellaro, L. Jiang, M. V. G. Dutt, E. Togan, A. S. Zibrov, A. Yacoby, R. L. Walsworth, and M. D. Lukin, Nanoscale magnetic sensing with an individual electronic spin in diamond, *Nature (London)* **455**, 644 (2008).
- [7] D. M. Toyli, C. F. de las Casas, D. J. Christle, V. V. Dobrovitski, and D. D. Awschalom, Fluorescence thermometry enhanced by the quantum coherence of single spins in diamond, *Proc. Natl. Acad. Sci. USA* **110**, 8417 (2013).
- [8] C. Mühlherr, V. O. Shkolnikov, and G. Burkard, Magnetic resonance in defect spins mediated by spin waves, *Phys. Rev. B* **99**, 195413 (2019).
- [9] D. M. Toyli, D. J. Christle, A. Alkauskas, B. B. Buckley, C. G. Van de Walle, and D. D. Awschalom, Measurement and Control of Single Nitrogen-Vacancy Center Spins above 600 K, *Phys. Rev. X* **2**, 031001 (2012).

- [10] G.-Q. Liu, X. Feng, N. Wang, Q. Li, and R.-B. Liu, Coherent quantum control of nitrogen-vacancy center spins near 1000 kelvin, *Nat. Commun.* **10**, 1344 (2019).
- [11] A. Franco and F. C. e Silva, High temperature magnetic properties of cobalt ferrite nanoparticles, *Appl. Phys. Lett.* **96**, 172505 (2010).
- [12] W. Zhao, Z. Liu, Z. Sun, Q. Zhang, P. Wei, X. Mu, H. Zhou, C. Li, S. Ma, D. He, P. Ji, W. Zhu, X. Nie, X. Su, X. Tang, B. Shen, X. Dong, J. Yang, Y. Liu, and J. Shi, Superparamagnetic enhancement of thermoelectric performance, *Nature (London)* **549**, 247 (2017).
- [13] A. Kumar, J. F. Scott, and R. S. Katiyar, Magnon Raman spectroscopy and in-plane dielectric response in BiFeO₃: Relation to the Polomska transition, *Phys. Rev. B* **85**, 224410 (2012).
- [14] A. Jarmola, V. M. Acosta, K. Jensen, S. Chemerisov, and D. Budker, Temperature- and Magnetic-Field-Dependent Longitudinal Spin Relaxation in Nitrogen-Vacancy Ensembles in Diamond, *Phys. Rev. Lett.* **108**, 197601 (2012).
- [15] J. Michl, J. Steiner, A. Denisenko, A. Bülau, A. Zimmermann, K. Nakamura, H. Sumiya, S. Onoda, P. Neumann, J. Isoya, and J. Wrachtrup, Robust and accurate electric field sensing with solid state spin ensembles, *Nano Lett.* **19**, 4904 (2019).
- [16] H. J. Mamin, M. H. Sherwood, and D. Rugar, Detecting external electron spins using nitrogen-vacancy centers, *Phys. Rev. B* **86**, 195422 (2012).
- [17] I. Lovchinsky, A. O. Sushkov, E. Urbach, N. P. de Leon, S. Choi, K. De Greve, R. Evans, R. Gertner, E. Bersin, C. Müller, L. McGuinness, F. Jelezko, R. L. Walsworth, H. Park, and M. D. Lukin, Nuclear magnetic resonance detection and spectroscopy of single proteins using quantum logic, *Science* **351**, 836 (2016).
- [18] J. Wang, F. Feng, J. Zhang, J. Chen, Z. Zheng, L. Guo, W. Zhang, X. Song, G. Guo, L. Fan, C. Zou, L. Lou, W. Zhu, and G. Wang, High-sensitivity temperature sensing using an implanted single nitrogen-vacancy center array in diamond, *Phys. Rev. B* **91**, 155404 (2015).
- [19] B. A. Myers, A. Ariyaratne, and A. C. Bleszynski Jayich, Double-Quantum Spin-Relaxation Limits to Coherence of Near-Surface Nitrogen-Vacancy Centers, *Phys. Rev. Lett.* **118**, 197201 (2017).
- [20] V. M. Acosta, E. Bauch, M. P. Ledbetter, C. Santori, K. M. C. Fu, P. E. Barclay, R. G. Beausoleil, H. Linget, J. F. Roch, F. Treussart, S. Chemerisov, W. Gawlik, and D. Budker, Diamonds with a high density of nitrogen-vacancy centers for magnetometry applications, *Phys. Rev. B* **80**, 115202 (2009).
- [21] J. Choi, S. Choi, G. Kucsko, P. C. Maurer, B. J. Shields, H. Sumiya, S. Onoda, J. Isoya, E. Demler, F. Jelezko, N. Y. Yao, and M. D. Lukin, Depolarization Dynamics in a Strongly Interacting Solid-State Spin Ensemble, *Phys. Rev. Lett.* **118**, 093601 (2017).
- [22] V. M. Acosta, E. Bauch, M. P. Ledbetter, A. Waxman, L.-S. Bouchard, and D. Budker, Temperature Dependence of the Nitrogen-Vacancy Magnetic Resonance in Diamond, *Phys. Rev. Lett.* **104**, 070801 (2010).
- [23] M. W. Doherty, V. M. Acosta, A. Jarmola, M. S. J. Barson, N. B. Manson, D. Budker, and L. C. L. Hollenberg, Temperature shifts of the resonances of the NV⁻ center in diamond, *Phys. Rev. B* **90**, 041201(R) (2014).
- [24] X.-D. Chen, C.-H. Dong, F.-W. Sun, C.-L. Zou, J.-M. Cui, Z.-F. Han, and G.-C. Guo, Temperature dependent energy level shifts of nitrogen-vacancy centers in diamond, *Appl. Phys. Lett.* **99**, 161903 (2011).
- [25] M. S. Liu, L. A. Bursill, S. Prawer, and R. Beserman, Temperature dependence of the first-order Raman phonon line of diamond, *Phys. Rev. B* **61**, 3391 (2000).
- [26] M. S. J. Barson, P. Reddy, S. Yang, N. B. Manson, J. Wrachtrup, and M. W. Doherty, Temperature dependence of the ¹³C hyperfine structure of the negatively charged nitrogen-vacancy center in diamond, *Phys. Rev. B* **99**, 094101 (2019).
- [27] M. B. Walker, A T⁵ spin-lattice relaxation rate for non-Kramers ions, *Can. J. Phys.* **46**, 1347 (1968).
- [28] A. Schweiger and G. Jeschke, *Principles of Pulse Electron Paramagnetic Resonance* (Oxford University Press on Demand, 2001).
- [29] J. F. Barry, J. M. Schloss, E. Bauch, M. J. Turner, C. A. Hart, L. M. Pham, and R. L. Walsworth, Sensitivity optimization for NV-diamond magnetometry, *Rev. Mod. Phys.* **92**, 015004 (2020).
- [30] E. C. Reynhardt, G. L. High, and J. A. van Wyk, Temperature dependence of spin-spin and spin-lattice relaxation times of paramagnetic nitrogen defects in diamond, *J. Chem. Phys.* **109**, 8471 (1998).
- [31] R. U. A. Khan, B. L. Cann, P. M. Martineau, J. Samartseva, J. J. P. Freeth, S. J. Sibley, C. B. Hartland, M. E. Newton, H. K. Dhillon, and D. J. Twitchen, Colour-causing defects and their related optoelectronic transitions in single crystal CVD diamond, *J. Phys.: Condens. Matter* **25**, 275801 (2013).
- [32] L. S. Hounsome, R. Jones, P. M. Martineau, D. Fisher, M. J. Shaw, P. R. Briddon, and S. Öberg, Origin of brown coloration in diamond, *Phys. Rev. B* **73**, 125203 (2006).
- [33] T. Feng and B. D. Schwartz, Characteristics and origin of the 1.681 eV luminescence center in chemical-vapor-deposited diamond films, *J. Appl. Phys.* **73**, 1415 (1993).
- [34] F.-F. Yan, J.-F. Wang, Q. Li, Z.-D. Cheng, J.-M. Cui, W.-Z. Liu, J.-S. Xu, C.-F. Li, and G.-C. Guo, Coherent Control of Defect Spins in Silicon Carbide above 550 K, *Phys. Rev. Appl.* **10**, 044042 (2018).
- [35] G. Balasubramanian, P. Neumann, D. Twitchen, M. Markham, R. Kolesov, N. Mizuochi, J. Isoya, J. Achard, J. Beck, J. Tissler, V. Jacques, P. R. Hemmer, F. Jelezko, and J. Wrachtrup, Ultra-long spin coherence time in isotopically engineered diamond, *Nat. Mater.* **8**, 383 (2009).
- [36] B. Naydenov, F. Dolde, L. T. Hall, C. Shin, H. Fedder, L. C. L. Hollenberg, F. Jelezko, and J. Wrachtrup, Dynamical decoupling of a single-electron spin at room temperature, *Phys. Rev. B* **83**, 081201(R) (2011).
- [37] N. Bar-Gill, L. Pham, A. Jarmola, D. Budker, and R. Walsworth, Solid-state electronic spin coherence time approaching one second, *Nat. Commun.* **4**, 1743 (2013).
- [38] H. Ishiwata, M. Nakajima, K. Tahara, H. Ozawa, T. Iwasaki, and M. Hatano, Perfectly aligned shallow ensemble nitrogen-vacancy centers in (111) diamond, *Appl. Phys. Lett.* **111**, 043103 (2017).
- [39] A. M. Edmonds, U. F. S. D'Haenens-Johansson, R. J. Cruddle, M. E. Newton, K. M. C. Fu, C. Santori, R. G. Beausoleil, D. J. Twitchen, and M. L. Markham, Production of oriented nitrogen-vacancy color centers in synthetic diamond, *Phys. Rev. B* **86**, 035201 (2012).